

# Enhanced Thermal and Mechanical Properties of 3D Printed Highly Porous Structures Based on $\gamma$ -Al<sub>2</sub>O<sub>3</sub> by Adding Graphene Nanoplatelets

Luis Moreno-Sanabria, Cristina Ramírez, María Isabel Osendi, Manuel Belmonte,\* and Pilar Miranzo\*

One of the main challenges to widen the potential applications of 3D printed highly porous ceramic structures in catalysis, energy storage or thermal management resides in the improvement of both their mechanical resistance and thermal conductivity. To achieve these goals, highly hierarchical  $\gamma$ -alumina ( $\gamma$ -Al<sub>2</sub>O<sub>3</sub>) scaffolds containing up to 18 vol% of graphene nanoplatelets (GNP), including channels of controlled size and shape in the millimeter scale and meso-porosity within the rods, are developed by robocasting from boehmite-based aqueous inks without other printing additives. These 3D structures exhibit high porosity (85%) and specific surface area of 100 m<sup>2</sup> g<sup>-1</sup>. The incorporation of 12 vol% GNP leads to an enhanced mechanical response of the scaffolds, increasing the compressive strength and the elastic modulus up to  $\approx$ 80% as compared with data for plain  $\gamma$ -Al<sub>2</sub>O<sub>3</sub> scaffolds. The thermal conductivity is measured by the transient plane source method using specifically designed 3D structures with external sidewalls and additional top/bottom covers to assure a good contact at the outer surfaces. The thermal conductivity of 3D porous structures augments with the GNP content, reaching a maximum value four times higher for the scaffolds containing 18 vol% GNP than that attained for the 3D monolithic  $\gamma$ -Al<sub>2</sub>O<sub>3</sub>.


## 1. Introduction

Within the category of porous ceramic materials, those based on transition alumina ( $\chi$ ,  $\eta$ ,  $\gamma$ ,  $\delta$ ,  $\kappa$ ,  $\theta$ -Al<sub>2</sub>O<sub>3</sub>), specially  $\gamma$ -Al<sub>2</sub>O<sub>3</sub>, stand out due to their chemical and thermal stability, well-developed porosity, high absorption capacity, controllable surface concentration of acidic and basic centers, low cost, commercial availability, and low toxicity.<sup>[1–5]</sup>  $\gamma$ -Al<sub>2</sub>O<sub>3</sub> nanostructures have proven their utility as adsorbents, catalysts, and bio-

logically active materials and, recently, in other emerging applications like flame retardants for polymers, quasi-solid electrolytes, or antimicrobial agents.<sup>[3]</sup> In particular, macroporous alumina with hierarchical pore structure, high surface area, and narrow pore size distribution are highly desirable for heterogeneous catalysts, as for example, hydrotreating catalysts used for heavy oils.<sup>[6–8]</sup> In this way, the catalytic performance can be enhanced through the development of suitable macrostructures of the catalysts, which depends on the support, reducing the mass transfer resistance, improving the reaction efficiency and increasing the lifetime of the catalysts. In this context, the additive manufacturing (AM) techniques allow developing highly hierarchical 3D structures that include channels of controlled size and shape in the millimeter scale, while porosity at meso- and micro-scales within the struts can be tailored using different strategies. Direct ink writing (DIW), an AM technology, allows building customized porous scaffolds with precise intricate geometries of a wide range of materials by computer controlling the scaffold parameters and adjusting the ink properties. DIW presents some drawbacks as compared to other AM technologies employed for porous ceramic scaffolds, such as stereolithography, in particular, poor surface quality of the 3D printed structures, which can be greatly improved by using smaller nozzle diameters, and, especially, the limitation to directly produce scaffolds with spanning, overhanging, and floating features that would require employing sacrificial supporting materials.<sup>[9–11]</sup>

Main concerns for the application of the 3D printed macroporous  $\gamma$ -Al<sub>2</sub>O<sub>3</sub> structures are its reduced mechanical resistance that may restrain their possible applications, and its limited heat transfer capability associated to the high porosity, which is particularly important in the case of 3D printed porous materials with applications in fields like catalysis, energy production and storage, and for thermal management as heat exchangers and heat sinks.<sup>[12–20]</sup> The incorporation of well-dispersed graphene nanostructures, 2D carbon allotropes with outstanding electronic and physiochemical properties,<sup>[21]</sup> into the  $\gamma$ -Al<sub>2</sub>O<sub>3</sub> matrix can increase both the mechanical and the thermal performance of 3D printed  $\gamma$ -Al<sub>2</sub>O<sub>3</sub> structures<sup>[22]</sup> and

L. Moreno-Sanabria, C. Ramírez, M. I. Osendi, M. Belmonte, P. Miranzo  
Institute of Ceramics and Glass (ICV-CSIC)  
Madrid 28049, Spain  
E-mail: mbelmonte@icv.csic.es; pmiranzo@icv.csic.es

 The ORCID identification number(s) for the author(s) of this article can be found under <https://doi.org/10.1002/admt.202101455>.

© 2022 The Authors. Advanced Materials Technologies published by Wiley-VCH GmbH. This is an open access article under the terms of the Creative Commons Attribution-NonCommercial-NoDerivs License, which permits use and distribution in any medium, provided the original work is properly cited, the use is non-commercial and no modifications or adaptations are made.

DOI: 10.1002/admt.202101455

could widen the application of these types of structures.<sup>[20]</sup> In fact, 3D structures based on  $\gamma\text{-Al}_2\text{O}_3$  and  $\alpha\text{-Al}_2\text{O}_3$  reinforced by 2 wt% of carbon nanotubes (CNT) or reduced graphene oxide (rGO) ribbons have recently been developed by robocasting, a DIW technique, employing boehmite gels.<sup>[23]</sup> The use of boehmite gels to develop printable inks while avoiding any other printing additives has demonstrated a great potential for DIW of ceramics.<sup>[12,23–28]</sup> The 3D  $\text{Al}_2\text{O}_3$  structures containing CNT and rGO exhibited superior mechanical properties while preserving high porosity and specific surface area.<sup>[23]</sup> However, processing inks with high concentrations of these carbon nanostructures might be problematic due to formation of agglomerates, and the reduced effectiveness in load transfer of the 1D-nanostructures compared to 2D-fillers could limit further improvements of the compressive strength.

Although the effect of graphene additions on the thermal conductivity was not evaluated for these highly porous 3D printed  $\gamma\text{-Al}_2\text{O}_3$  structures, significant enhancement in the heat dissipation of chemical reactions has been reported for  $\gamma\text{-Al}_2\text{O}_3/\text{rGO}$  nanostructures, being excellent catalyst supports for poly(ethylenimine) aimed at  $\text{CO}_2$  removal.<sup>[29]</sup> Other interesting features reported for  $\gamma\text{-Al}_2\text{O}_3/\text{rGO}$  nanostructures were the enhanced photocatalytic activity under solar light for decomposing certain organics<sup>[30]</sup> and the good electrochemical performance for ascorbic acid sensing.<sup>[31]</sup>

On the other hand, the incorporation of graphene nanoplatelets (GNP) as fillers, which are better electrical and thermal conductors than either rGO nanoplatelets or nanoribbons, and can be added in higher concentrations,<sup>[22]</sup> would allow simultaneous improvements of the thermal performance and the mechanical response of highly porous  $\gamma\text{-Al}_2\text{O}_3$  structures. Another important advantage of GNP additions to take into account is its catalytic performance. Quintanilla et al.<sup>[32]</sup> demonstrated that GNP exhibited much higher catalytic activity than GO in the wastewater treatment using catalytic wet peroxide oxidation processes. The presence of low amount of surface oxidation groups in GNP, as compared to GO, enhanced the electron mobility to decompose the hydrogen peroxide and, hence, improved the efficiency of the catalytic reaction. Despite these promising outlooks, the development of highly porous 3D structures based on  $\gamma\text{-Al}_2\text{O}_3/\text{GNP}$  composites has not been reported hitherto. In this work, we have robocast light and robust 3D printed cellular  $\gamma\text{-Al}_2\text{O}_3$  composite structures with up to 18 vol% of GNP looking for improved structural and functional properties, in particular, the thermal conductivity and some key mechanical properties. The porosity of the scaffolds has been structured hierarchically, where the macroporosity has been built through the patterned design and the porosity at a meso-micro scale has been created by adjusting the sintering temperature of the scaffolds. The role played by increasing amounts of GNP in the rheological properties of the inks, and the microstructure and final properties of the 3D structures, have been deeply studied.

## 2. Results and Discussion

Boehmite commercial powders and functionalized GNP were employed to prepare  $\gamma\text{-Al}_2\text{O}_3$ -based materials with GNP contents

**Table 1.** Composition of the different boehmite-based inks (in vol%) and the corresponding vol% of GNP into the 3D printed and thermal treated  $\gamma\text{-Al}_2\text{O}_3$ -based materials, including their labels.

Label	Ink composition [vol%]			Materials composition [vol%]	
	Boehmite	GNP	H <sub>2</sub> O	$\gamma\text{-Al}_2\text{O}_3$	GNP
0GNP	26.5	0	73.5	100	0
6GNP	25.4	1.4	73.2	94.0	6.0
12GNP	24.3	2.8	72.9	88.1	11.9
18GNP	23.2	4.2	72.6	82.2	17.8

of 0, 6, 12, and 18 vol% (labeled as 0GNP, 6GNP, 12GNP, and 18GNP). Highly concentrated inks for both the monolithic  $\gamma\text{-Al}_2\text{O}_3$  material and the  $\gamma\text{-Al}_2\text{O}_3/\text{GNP}$  composites were fabricated by adding to an initial stable aqueous dispersion of 41 wt% of boehmite the required amount of the corresponding powders (boehmite and GNP). The final composition of the printable inks is collected in **Table 1**. They contained  $\approx 73$  vol% of ultrapure water and  $\approx 27$  vol% of solids ( $\approx 52$  wt%), and additional electrolyte type additives were not necessary for the appropriate printability of the inks. The apparent viscosity ( $\eta$ ) of these inks versus the shear rate ( $\dot{\gamma}$ ) is plotted in **Figure 1a**; showing a clear shear thinning behavior with  $\eta$  values decreasing by about three orders of magnitude for  $\dot{\gamma}$  increasing from 0.1 to 100  $\text{s}^{-1}$ . This behavior ensures good printability as the inks reached sufficiently low  $\eta$  during the extrusion at low pressures through the nozzle tip, while high  $\eta$  values were attained after tension removal as they exit the nozzle, which ensures filaments stiffness. A high storage modulus ( $G' \approx 10^5$  Pa) and yield stress ( $\tau_y \approx 10^3$  Pa) (**Figure 1b**) were measured for the boehmite/GNP composite inks. Although GNP additions to boehmite lead to inks with almost one order of magnitude higher shear moduli, as compared to  $G'$  and  $G''$  of the 0GNP ink, values of  $G'$  diminish with the GNP content at high shear stresses (above 200 Pa), which is probably due to the increasing GNP orientation with the  $a$ - $b$  plane parallel to the applied stress direction as  $\dot{\gamma}$  rises during the test. In this way, the intersection of  $G'$  and  $G''$  takes place at progressively lower shear stress as GNP increases and, consequently,  $\tau_y$  lowers with the GNP content from  $3 \times 10^3$  Pa, for the plain boehmite ink, to  $0.5 \times 10^3$  Pa, for the ink with 18GNP (**Figure 1c**). Similar decrease in  $\tau_y$  has also been reported for  $\text{Al}_2\text{O}_3$  inks based on mixtures of spherical and platelet-like particles where the platelet contents were higher than 20 vol%, also showing  $\tau_y$  values below  $0.6 \times 10^3$  Pa.<sup>[33]</sup>

3D square structures (scaffolds) were printed with a three-axis robocasting system extruding through the nozzle tip of 840  $\mu\text{m}$  inner diameter linear arrays of parallel rods (struts) in the  $x$ - $y$  plane that are perpendicularly piled in the  $z$  direction. A 3D CAD software was employed to design specific specimens for the measurement of the different properties. In this way, as it is shown in **Figure 2a**, the scaffolds used for the thermal and electrical conductivity characterization (Type 1) had large dimensions ( $30 \times 30 \times 7.3$   $\text{mm}^3$ ), external sidewalls and additional top and bottom covers to assure a good contact at the outer surfaces. This is important to limit contact resistances at the heat source/specimen interface in the case of thermal characterization; while it simplifies the electrodes setting in the case of electrical conductivity testing. On the other

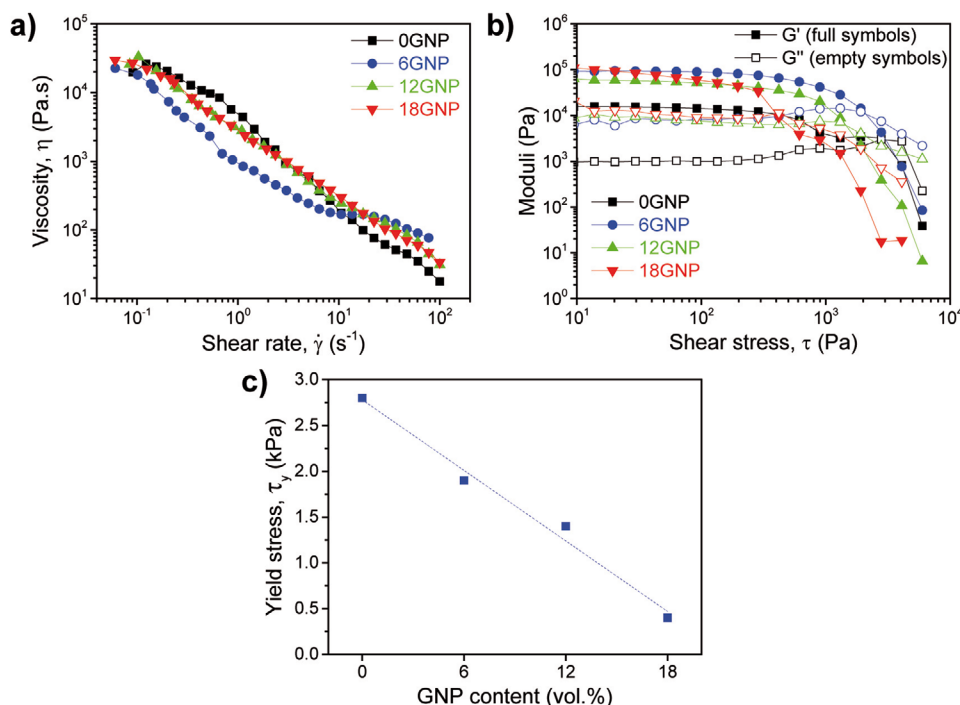


**Figure 1.** a) Apparent viscosity ( $\eta$ ) versus shear rate ( $\dot{\gamma}$ ) of plain boehmite and boehmite/GNP composite inks. b) Storage ( $G'$ , full symbols) and loss ( $G''$ , empty symbols) moduli as a function of the shear stress ( $\tau$ ) for the same inks. c) Plot of the yield stress ( $\tau_y$ ) versus the graphene content in the ink.

hand, cubic scaffolds of  $10 \times 10 \times 10 \text{ mm}^3$  without external walls (Type 2) were used in the mechanical tests, according to the recommendations for the compressive testing of cellular materials, included in ASTM D1621 – 16 and ISO 13314:2011 standards. It should be pointed that the tested volume is representative of the materials that includes 36 square cells in the  $x$ - $y$  plane with a total number of cuboid cells close to 300. The characteristic parameters that define the interior lattice structures (Figure 2a) are the rod diameter ( $\varnothing$ ), the distance between the centers of the adjacent rods ( $a$ ), and the distance between two equivalent

layers in the  $z$  direction ( $h$ ), initially fixed in the as-printed state as 0.82 (resulting from the inner diameter of the nozzle tip), 1.67, and 1.27 mm, respectively. The shape retention of the printed structures is confirmed in Figure 2b. Although the boehmite ink has one order of magnitude lower shear moduli, its yield stress was higher than that of the composite inks (Figure 1c) and the  $\gamma\text{-Al}_2\text{O}_3$  structures also preserved the shape of the filaments without any significant damage. The as-printed 3D scaffolds were slowly dried under ambient conditions and, then, at  $100^\circ\text{C}$  to prevent crack formation. Based on the

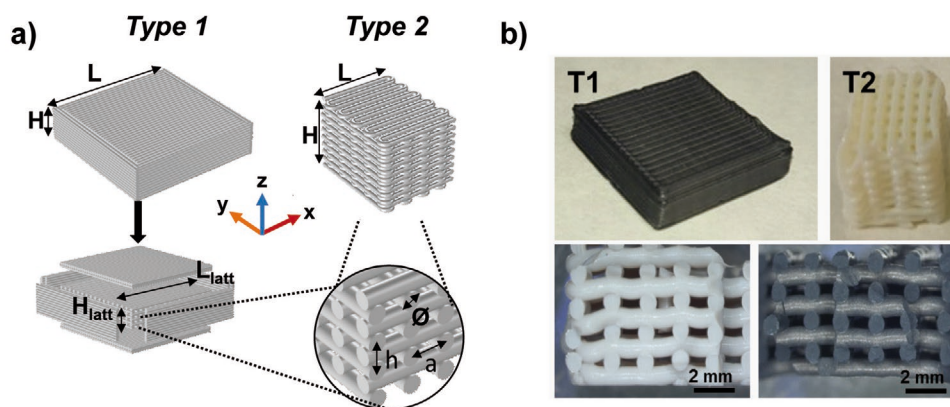


**Figure 2.** a) CAD models for the distinct structures. Type 1: enclosed by sidewalls and additional top and bottom covers for the thermal and electrical conductivity measurements, with dimensions of  $30 \times 30 \times 7.3 \text{ mm}^3$ , and Type 2: without external sidewalls and dimensions of  $10 \times 10 \times 10 \text{ mm}^3$  used in the mechanical tests. The characteristic parameters of the elemental lattice, that is, rod diameter ( $\varnothing$ ), distance between the centers of the adjacent rods ( $a$ ), and distance between two equivalent layers in the  $z$  direction ( $h$ ) are pointed out in the inset. b) Top images showing examples of as-printed structures of Types 1 (T1) and 2 (T2) corresponding to 12GNP and 0GNP, respectively; while bottom images are T2 fractured structures of 0GNP (left) and 12GNP (right) scaffolds where the rod shape retention is observed.

thermogravimetric analysis of GNP and original boehmite powders included in Figure S1, Supporting Information, a thermal treatment at 500 °C for 2 h under nitrogen was selected to avoid GNP degradation and assure a complete transformation of boehmite into  $\gamma\text{-Al}_2\text{O}_3$ . These conditions maintained high porosity and specific surface area of the scaffolds, as well as sufficient mechanical strength for handling.

In parallel, the extruded inks were also cast into a cylindrical mold and slightly uniaxially pressed to get compacts (referred to as “bulk materials” hereinafter) of same compositions as the 3D structures, which were equally dried and heat treated.

The transformation of boehmite into  $\gamma\text{-Al}_2\text{O}_3$  was confirmed by X-ray diffraction (XRD) in both the 3D structures (Figure 3a) and the bulk specimens (included in the Figure S2, Supporting Information), where the diffraction peaks associated to the crystalline  $\gamma$  phase are clearly identified. On the other hand, peaks corresponding to graphite are also detected in the composites, especially the most intense (002) diffraction peak. A summary of the average Raman spectra acquired on  $20 \times 20 \mu\text{m}^2$  areas of the rod surface for different 3D printed materials is included in Figure S3, Supporting Information. Although the micro-Raman spectrum of monolithic  $\gamma\text{-Al}_2\text{O}_3$  is featureless, Raman peaks associated to the D, G, and 2D bands of GNP are clearly distinguishable overlaying the fluorescence band produced by the porous surface in the spectra of the  $\gamma\text{-Al}_2\text{O}_3$ /GNP composites. The Raman intensity maps of the 18GNP sample are included in Figure 3b as an example, representing zones with a more intense D band and zones with an intense G band. The average integrated area ratio of D and G bands ( $I_D/I_G$ ) was 0.30 for the composites, slightly above than that of pristine GNP (0.15), which indicates that there was not significant degradation of the nanoplatelets during ink processing and the further heat treatment at 500 °C. In agreement with this result, D band maps showed higher intensity for zones associated with lattice disorder at the platelets edges. On the other hand, red shifts of the G band position from  $1570 \text{ cm}^{-1}$  of the pristine GNP to  $1567 \text{ cm}^{-1}$  for the 12GNP and 18GNP composites were detected (Figure 3c), which differ from the blue shift observed in the as-printed 12GNP (boehmite matrix) and in other ceramic/graphene composites, attributed to the development of a compressive strain on the basal *ab*-plane of the GNP induced during cooling by the ceramic matrix.<sup>[34–36]</sup> Therefore, blue and red shifts are influenced by matrix structural changes due to the dehydration treatment. The observed lowering of the Raman frequency in the composite scaffolds could be attributed to a decreasing of the vibration energy by reducing the van der Waals forces between graphene sheets, which can be ascribed to the development of tensile strains, expanded GNP layers due to its surface modification, or even to GNP charge doping, as some authors have proposed.<sup>[37–39]</sup>

Important volume shrinkages of the as-printed scaffolds were observed only during the drying process; while dimensions of the 3D specimens remained almost constant after the heat treatment at 500 °C. Type 1 and 2 scaffolds showed final isotropic shrinkages of 15%. The average weight loss observed during the thermal process under nitrogen flow was around 14%, although it slightly decreased with the GNP content; in fact, the weight loss for the monolithic  $\gamma\text{-Al}_2\text{O}_3$  was 14.6%;

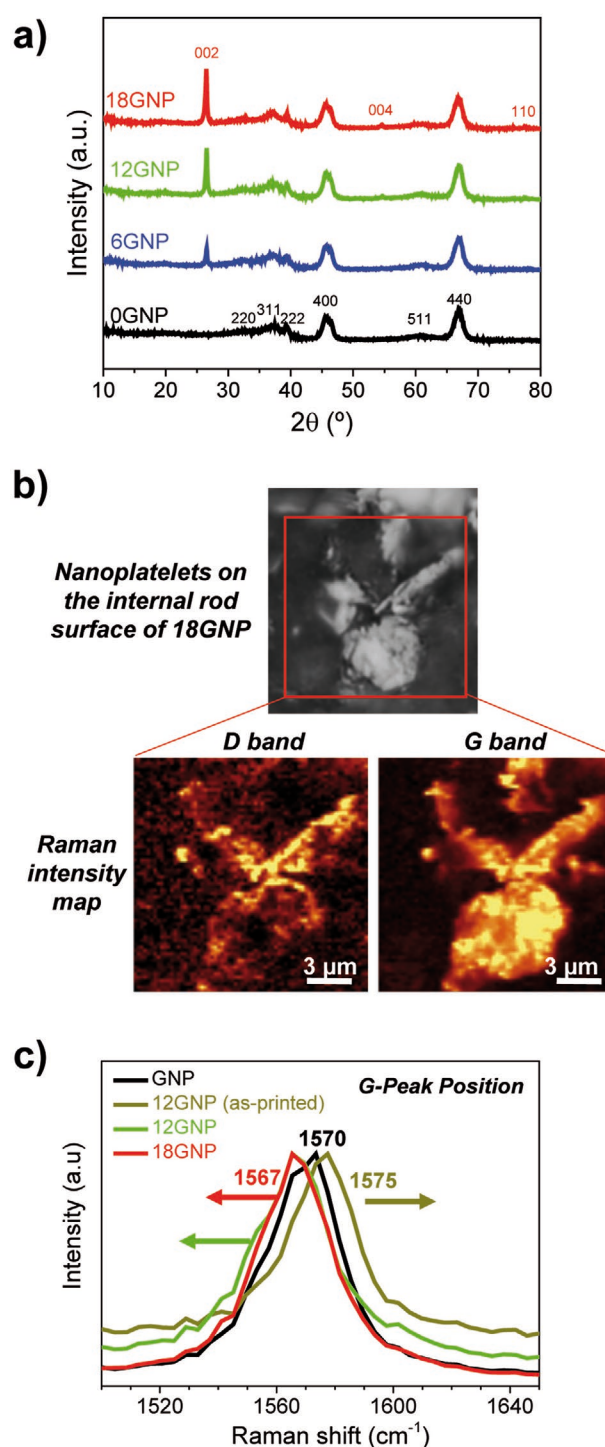


**Figure 3.** a) XRD patterns of the powered 3D materials including diffraction peaks of  $\gamma\text{-Al}_2\text{O}_3$  in the pattern of 0GNP and those of graphite in the pattern of 18GNP. b) Optical image of nanoplatelets on the internal rod surface of 18GNP and the corresponding Raman intensity maps of the scanned area (inside the frame) for D and G bands, D band being associated to disorder at platelets edges. c) G peak position for pristine GNP and 12GNP and 18GNP composite scaffolds, where 12GNP in its as-printed shape (boehmite matrix) has also been included.

**Table 2.** Parameters defining interior lattice of the scaffolds according to Figure 2, geometrical density ( $\rho_{\text{geo}}$ ), total porosity ( $\pi_{\text{total}}$ ), fraction of macropores ( $\pi_{\text{macro}}$ ), and porosity of the rods ( $\pi_{\text{solid}}$ ), for both type of structures as well as for the bulk reference materials.

		0GNP	6GNP	12GNP	18GNP
Lattice parameters	$\varnothing$ [mm]	0.74	0.74	0.77	0.77
	A [mm]	1.58	1.58	1.59	1.59
	h [mm]	1.10	1.10	1.12	1.12
$\rho_{\text{geo}}$ [ $\text{g cm}^{-3}$ ]	Bulk	0.99	1.05	1.05	1.07
	Type 1	0.81	0.80	0.80	0.78
	Type 2	0.51	0.50	0.50	0.50
$\pi_{\text{total}}$	Bulk	0.73	0.71	0.70	0.68
	Type 1	0.78	0.78	0.77	0.77
	Type 2	0.86	0.86	0.86	0.85
$\pi_{\text{macro}}$	Type 1	0.23	0.21	0.20	0.21
	Type 2	0.41	0.42	0.38	0.37
$\pi_{\text{solid}}$	Type 1	0.71	0.71	0.71	0.71
	Type 2	0.75	0.76	0.76	0.74

whereas it reduced to 12.3 wt% for 18GNP. This value matches the weight loss of the 82 vol%  $\gamma\text{-Al}_2\text{O}_3$  present in this composite. The specimens were highly porous, with density values of  $\approx 1.0 \text{ g cm}^{-3}$  for bulk materials,  $\approx 0.8 \text{ g cm}^{-3}$  for the Type 1 scaffolds, and  $\approx 0.5 \text{ g cm}^{-3}$  for the Type 2 ones. Table 2 summarizes data for the density and different kinds of porosity calculated for each type of scaffold according to equations detailed in the Experimental Section. The porosity for the lattices (interior spanned structure in the case of the Type 1 covered scaffolds) was around 40% for all scaffolds but the fraction of macropores ( $\pi_{\text{macro}}$ ), referred to the whole structure, depends on the CAD design, reducing to  $\approx 20\%$  in the case of the Type 1 due to the inclusion of the covering layers. In a similar way, the total porosity of the scaffolds,  $\pi_{\text{total}}$ , is also slightly ( $\approx 9\%$ ) lower in Type 1 scaffolds than in Type 2 ones; however, as expected, the solid phase forming rods has similar porosity in both types of structures. According to Table 2, porosity data for bulk materials are close to those of solid phase in the printed scaffolds and, therefore, they can be used as a reference for the rod properties.

The hysteresis observed in the  $\text{N}_2$  adsorption–desorption isotherms for the scaffolds (Figure 4a) can be associated to the nitrogen capillary condensation inside meso-pores. The pore size distributions (Figure 4b) according to the Barrett-Joyner-Halenda (BJH) model evidence the occurrence of a peak at 20–25 nm in these materials linked to the mesoporosity. The BET specific surface area ( $S_e$ ) is quite high and close to that of the initial boehmite powder ( $100 \text{ m}^2 \text{ g}^{-1}$ ), and the presence of GNP slightly decreases  $S_e$  from 102 (0GNP) to  $94 \text{ m}^2 \text{ g}^{-1}$  (18GNP) and results in a slightly lower BJH average pore diameter (from 13 to 10 nm, respectively). The total pore volume in the pore diameter range of 1.7–300 nm decreased from 0.27 to  $0.17 \text{ cm}^3 \text{ g}^{-1}$  for graphene contents varying between 0 and 18 vol%. Mercury intrusion porosimetry was also employed to complete the porosity study, analyzing the presence of pores in a wider range that included

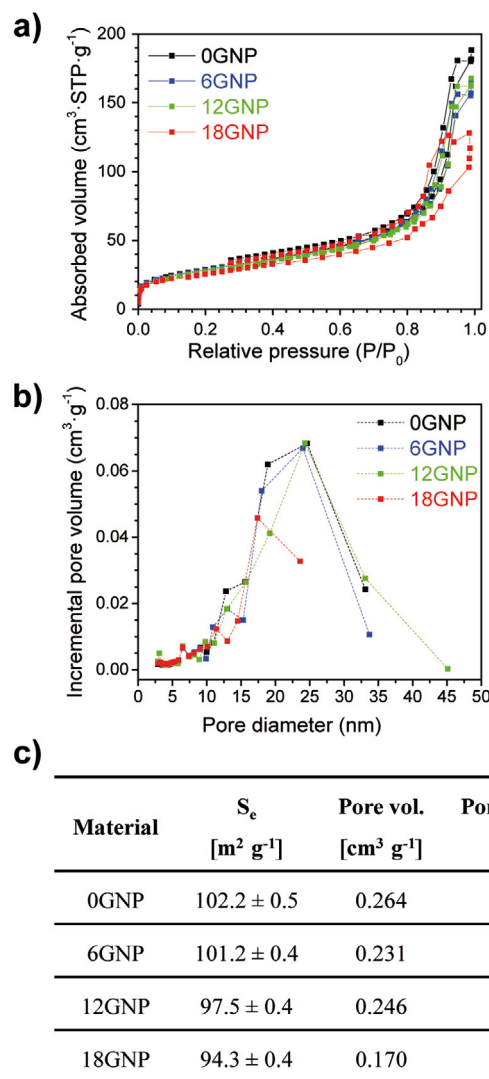


**Figure 4.** a)  $\text{N}_2$  adsorption/desorption isotherms for the scaffolds showing certain hysteresis in all materials, b) BJH pore size distribution calculated from the desorption branch, and c) table summarizing BET specific surface area ( $S_e$ ), total volume of pores with sizes between 1.7 and 300 nm, and average pore diameter according to the BJH model.

values above 50 nm (Figure S4, Supporting Information). As seen, pore distributions agree with the  $\text{N}_2$  adsorption–desorption data being centered at 27 nm. Besides, the scaffolding materials do not contain pores above 200 nm, although some porosity, mainly in the range of 50–100 nm, is also found, being slightly higher for 18GNP than for the rest of materials.

The microstructural observations by field emission scanning electron microscopies (FESEM) of the cross section of fractured rods are presented in Figures 5 and 6. As seen in Figure 5 through some representative examples, GNP does not significantly affect the matrix grain growth and rods forming the scaffolds contain very fine  $\gamma\text{-Al}_2\text{O}_3$  grains of less than  $\approx 100 \text{ nm}$  in all the cases. The good dispersion of the GNP within the matrix is evidenced in Figure 6, where it can be observed that GNP appear oriented with their  $a$ – $b$  plane parallel

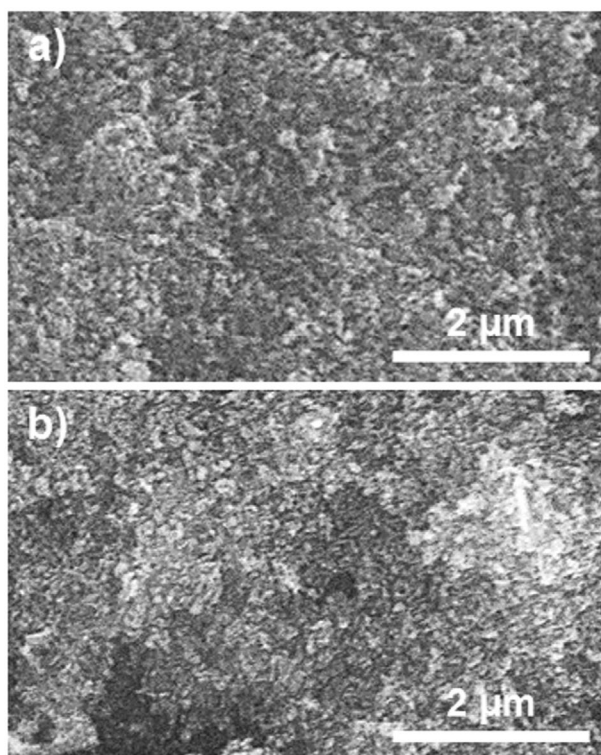


**Figure 5.** FESEM micrographs of the cross section of fractured rods corresponding to the  $\gamma\text{Al}_2\text{O}_3$  matrix for 3D structures: a) 0GNP and b) 18GNP.

to the rod axis due to the shear stresses developed during the printing process of the corresponding ink.

Considering that some water absorption from the environmental moisture could be expected for structures like the present ones, that is, with high porosity and  $S_e$ , weight loss was also analyzed by thermogravimetric differential thermal analysis (TGA-DTA) for the samples after the heat treatment at 500 °C (Figure S5, Supporting Information). The TGA profiles clearly show a weight loss of around 6% centered at  $\approx 100$  °C and compatible with the mentioned water absorption. That weight loss slightly decreased with the GNP content and, then, it is mainly related to the fraction of the highly porous  $\gamma\text{Al}_2\text{O}_3$  matrix in the composites. The 6% of absorbed water agrees with experimental observations and mathematical models for nanostructured materials with meso-pores<sup>[40]</sup> when the relative humidity is below 0.8 (laboratory ambient conditions). As it can be seen in the differential scanning calorimetry (DSC) curves of **Figure 7a**, the absorbed water affects the heat capacity of the 3D  $\gamma\text{Al}_2\text{O}_3$ /GNP materials; a wide hump centered at  $\approx 100$  °C can be observed in the first cycle that disappears in the following runs (Figure 7b), and the specific heat ( $C_p$ ) at room temperature slightly higher for the first test ( $\approx 1000$  vs  $\approx 750$  J kg<sup>-1</sup> K<sup>-1</sup> of the subsequent runs). These  $C_p$  values agree with those calculated by the rule of mixtures from  $C_p$  data reported in the literature for GNP and  $\gamma\text{Al}_2\text{O}_3$ .<sup>[41,42]</sup> The  $C_p$  calculated for each composition is collected in Table S1, Supporting Information. Figure 7c includes the thermal conductivity ( $\kappa$ ) of the scaffolds and the corresponding bulk materials. In the first case,  $\kappa$  was measured just by transient plane source

(TPS) method due to the high porosity of the 3D materials, while the bulk materials were characterized by both TPS and the laser flash technique. It should be noted that, in this case, the thermal diffusivity ( $\alpha$ ) and  $\kappa$  values seem to be quite consistent when comparing the two testing methods, and both significantly increased with the GNP content,  $\alpha$  varying from  $1.5 \times 10^{-7}$  to  $3.5 \times 10^{-7}$  mm<sup>2</sup> s<sup>-1</sup> and  $\kappa$  from 0.10 to 0.37 W m<sup>-1</sup> K<sup>-1</sup> for GNP contents in the 0 to 18 vol% range. In this way, the thermal conductivity of 18GNP composite was almost four times higher than that of the monolithic  $\gamma\text{Al}_2\text{O}_3$ .

The 3D structures show the same trend but have significantly reduced thermal conductivity values, which is a consequence of their higher porosity. In particular, data for the scaffolds are about 0.7 times lower than the corresponding bulk materials. On the other hand,  $\alpha$  values for the scaffolds are slightly lower than those of the bulk materials (Figure 7b) as their densities (0.74–0.79 times the density of the bulk materials, Table 2) decrease in similar proportion as the thermal conductivity. The effect of the macroporosity on the effective thermal conductivity of the scaffolds has been analyzed by applying the simple exponential Pabst's model.<sup>[43]</sup>

$$\frac{\kappa}{\kappa_0} = e^{-1.5 \frac{\pi_{\text{macro}}}{1 - \pi_{\text{macro}}}} \quad (1)$$

where  $\kappa_0$  would be the thermal conductivity of the rod material, that is, that of the bulk material. When introducing the  $\pi_{\text{macro}}$  values of the Type 1 structures, which are between 0.18 and 0.21 (Table 2) in Equation (1),  $\kappa/\kappa_0$  ratios in the range of 0.69–0.72 are estimated, similar to the experimental  $\kappa/\kappa_0$  values by TPS. Figure 7d collects the information found in the literature for thermal conductivity of 3D porous materials manufactured by printing methods where the relative thermal conductivity ( $\kappa/\kappa_0$ ) referred to the rod thermal conductivity is plotted versus the percentage of voids. Despite it being difficult to make a real comparison with  $\kappa$  data reported for distinct 3D printed materials, namely metals and polymers, due to the multitude of printing variables affecting their structuring features as well as the different thermal conductivity measurement methods, data approximate the exponential Equation (1) when identifying the  $\pi_{\text{macro}}$  (present work) to the void fraction, which is the parameter commonly used in fused deposition modeling (FDM). Most of the data included in Figure 7d correspond to materials fabricated by FDM using metal and polymer filaments (empty symbols in Figure 7d), and methods used for measuring the thermal conductivity varied between the TPS<sup>[44]</sup> for which the average  $\kappa$  (calculated as  $\sqrt{\kappa_x \kappa_z}$  from the reported data) was represented, and the heat flow meter<sup>[45,46]</sup> and the guarded hot-plate,<sup>[47]</sup> both providing values of  $\kappa_z$ . On the other hand, data for 3D ceramic scaffolds manufactured by robocasting (full symbols in Figure 7d) were estimated from high resolution infrared thermography.<sup>[48]</sup>

The electrical conductivity ( $\sigma_e$ ) of composite scaffolds varied from 10<sup>-6</sup> S m<sup>-1</sup>, for 6GNP and 12GNP, to 10<sup>-4</sup> S m<sup>-1</sup>, for 18GNP, and, therefore, they are seven to nine orders of magnitude higher than the insulating  $\gamma\text{Al}_2\text{O}_3$  matrix. These values are comparatively lower than those observed for other ceramic/graphene composite-based scaffolds<sup>[22]</sup> due to the exceptional porosity attained for the  $\gamma\text{Al}_2\text{O}_3$  matrix.

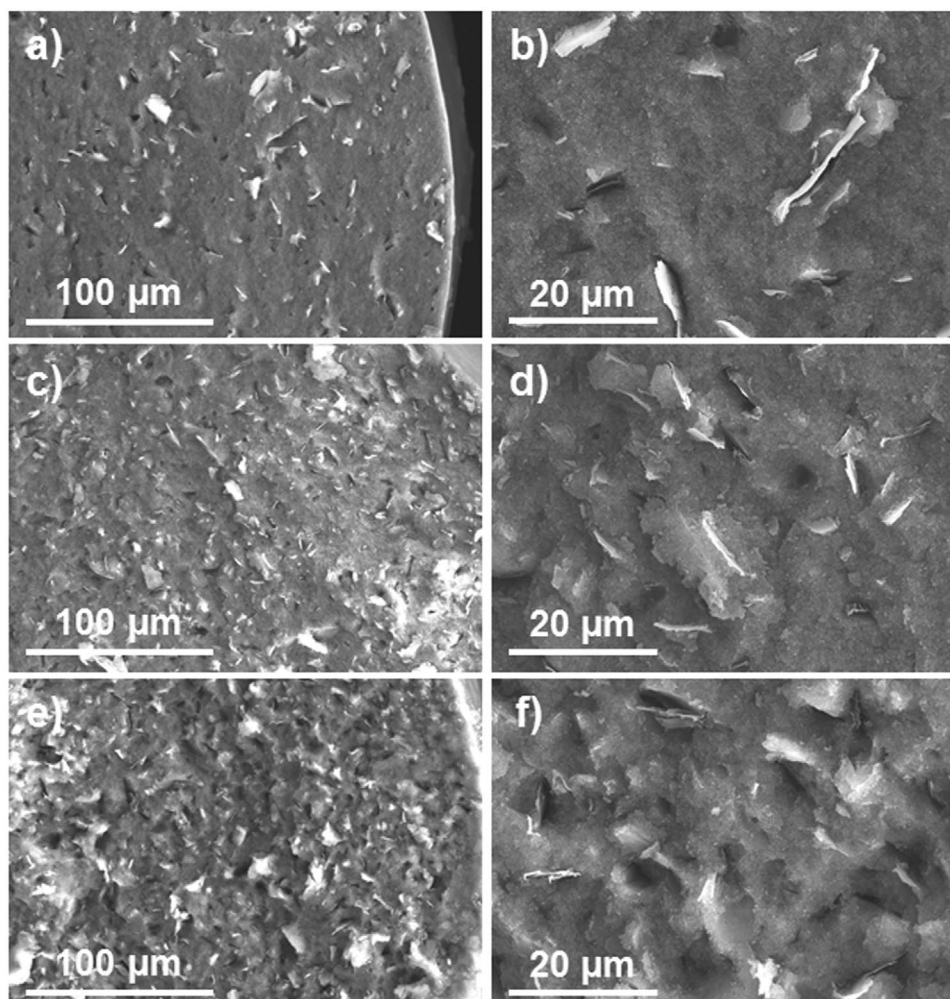


**Figure 6.** FESEM micrographs at different magnifications of the cross section of fractured rods of composite scaffolds: a,b) 6GNP, c,d) 12GNP, and e,f) 18GNP.

The compressive mechanical response of Type 2 structures is summarized in **Figure 8a**, where representative stress–strain curves for 0GNP, 6GNP, 12GNP, and 18GNP are plotted. All scaffolds exhibited the usual compressive behavior of cellular materials. In this way, the initial region is associated to the first layer flattening and the second region corresponds to an initial linear elastic region linked to the deformation of the cells up to reaching a maximum compressive strength (crushing point). Finally, the gradual collapse of the cells evidenced by the stress peaks registered during the tests leads to a progressive decrease in the retained strength while the strain augmented. As seen in **Figure 8a**, the plain  $\gamma\text{-Al}_2\text{O}_3$  scaffold showed a more catastrophic failure than the composite scaffolds, with a low contribution of the third region; while the composite scaffolds were more damage resistant and exhibited a clear progressive degradation with increasing stress. These phenomena were followed by simultaneously recording images of the composite scaffolds during the tests that illustrate the damage evolution, which are presented in **Figure 8b,c**. These figures collect some examples of stress–strain curves of 6GNP and 12GNP scaffolds and the corresponding images of

the specimens for each region of the curves. In this way, the first cracks initiated in both composite scaffolds in regions I and II of the curves, faster propagating through the whole structure in 6GNP scaffold. After the crushing point, some struts fractured (region III) leading to the progressive failure and collapse of the scaffold (regions IV–VI). This process was more dramatic in 6GNP than in 12GNP, which implies that larger GNP contents (12GNP) induce stronger reinforcement, arresting further crack propagation that produces a second stress peak and additional deformation before the complete structure collapses.

This high reinforcing effect of the  $\gamma\text{-Al}_2\text{O}_3$  material by incorporating 6–18 vol% of GNP promoted compressive strength ( $\sigma_c$ ) increases up to  $\approx 80\%$ , from  $\sigma_c = 0.37$  MPa for the 0GNP scaffold to  $\sigma_c = 0.67$  MPa for the 12GNP one, and increases the maximum strain during fracture from 4% (0GNP) to values above 12% (all composites). Moreover, the apparent elastic modulus ( $E$ ) of the composites also augments up to  $\approx 80\%$  over the value of the reference  $\gamma\text{-Al}_2\text{O}_3$  scaffold (**Figure 9a**).

Compressive response, as other mechanical properties, that is, elastic modulus and tensile strength, is strongly

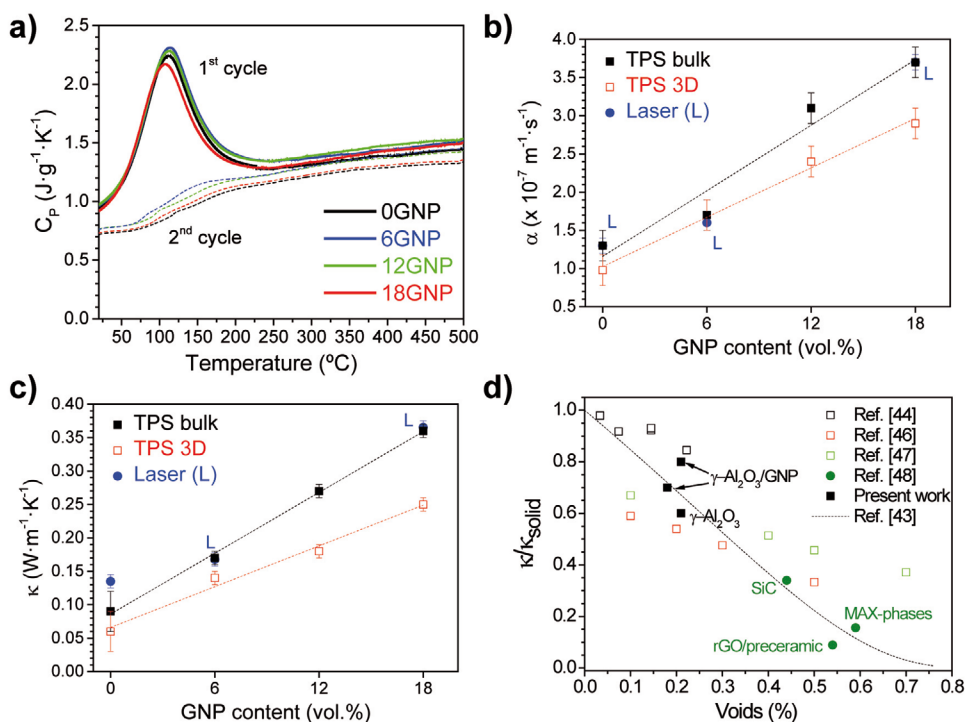


**Figure 7.** Results on thermal characterization: a) specific heat ( $C_p$ ) versus temperature measured by DSC for the different materials, where data for the first cycle (1<sup>st</sup>) and the average of subsequent three cycles (2<sup>nd</sup>) are plotted; b) thermal diffusivity ( $\alpha$ ) as a function of the GNP content for bulk materials and scaffolds measured by TPS; c) thermal conductivity ( $\kappa$ ) versus GNP content for bulk materials and scaffolds measured by TPS; and d) plot representing the relative thermal conductivity ( $\kappa/\kappa_0$ ) referred to the rod thermal conductivity versus the percentage of voids for different 3D porous materials manufactured by printing methods. Materials fabricated by FDM using metal and polymer filaments correspond to empty symbols; whereas data for 3D ceramic scaffolds manufactured by robocasting are represented using full symbols. The  $\alpha$  values measured by the laser flash method and the corresponding  $\kappa$  values assessed using DSC  $C_p$  values for 0GNP, 6GNP, and 18GNP bulk materials are also plotted in (b) and (c) (blue colored symbols).

influenced by porosity. Thus, in Figure 9b, the results obtained in the present work are compared with the compressive strength of different boehmite-based materials reported in literature,<sup>[23,49–52]</sup> with applications as catalytic supports. Both  $\gamma\text{-Al}_2\text{O}_3$  and  $\gamma\text{-Al}_2\text{O}_3/\text{GNP}$  scaffolds showed a behavior comparable to other  $\gamma$ -phase 3D structures processed at similar temperature or even to highly porous  $\alpha\text{-Al}_2\text{O}_3$  scaffolds. The marked difference with the bulk materials highlights the importance of finding a compromise between functionality and structural integrity, above all in the development of novel 3D catalytic reactors.<sup>[53,54]</sup>

The inspection by FESEM of samples after compression tests gave more insight on the causes of the good mechanical response of the composite scaffolds. Representative images of fractured scaffolds are depicted in Figure 10. A crushed cell showing a cross-sectional fractured rod and a visible crack developed on the surface of the orthogonal rod can be observed in Figure 10a. The magnified image of one of these cracks (Figure 10b) shows the occurrence of GNP pullout far from the crack tip. A platelet bridging crack face is detailed in Figure 10c and GNP protruding more than 10  $\mu\text{m}$  from the rod fracture surface are presented in Figure 10d. These observations support the occurrence of several toughening mechanisms typical of ceramic/GNP composites,<sup>[22,55]</sup> which are responsible for the increased mechanical strength of the  $\gamma\text{-Al}_2\text{O}_3/\text{GNP}$  composite scaffolds.

A good approximation of compressive and elastic behaviors for the values obtained in the present work could be done using the following equations:<sup>[56]</sup>

$$\frac{E}{E_s} = C_3 \left( \frac{\rho}{\rho_s} \right)^2 \quad (2)$$

$$\sigma_f = C_7 \sigma_{f_s} \left( \frac{\rho}{\rho_s} \right)^{1.5} \quad (3)$$

where  $E_s$  and  $\sigma_f$  are the elastic modulus and compressive strength of the rods, respectively,  $C_3$  and  $C_7$  are geometric constants, and  $\rho/\rho_s$  ( $\rho_{\text{Type2}}/\rho_{\text{bulk}}$  in Table 2) is the normalized density. The geometric constants were taken from experimental works on  $\text{Al}_2\text{O}_3$  cellular materials,<sup>[56]</sup> giving values very close to the measured data, that is,  $E = 30$  MPa and  $\sigma_f = 0.24$  MPa for 0GNP scaffolds, and  $E = 37$  MPa and  $\sigma_f = 0.35$  MPa for 12GNP one. More detailed calculation is presented in Table S2, Supporting Information.

### 3. Conclusions

$\gamma\text{-Al}_2\text{O}_3/\text{GNP}$  scaffolds showing patterned structure according to the design have successfully been manufactured by



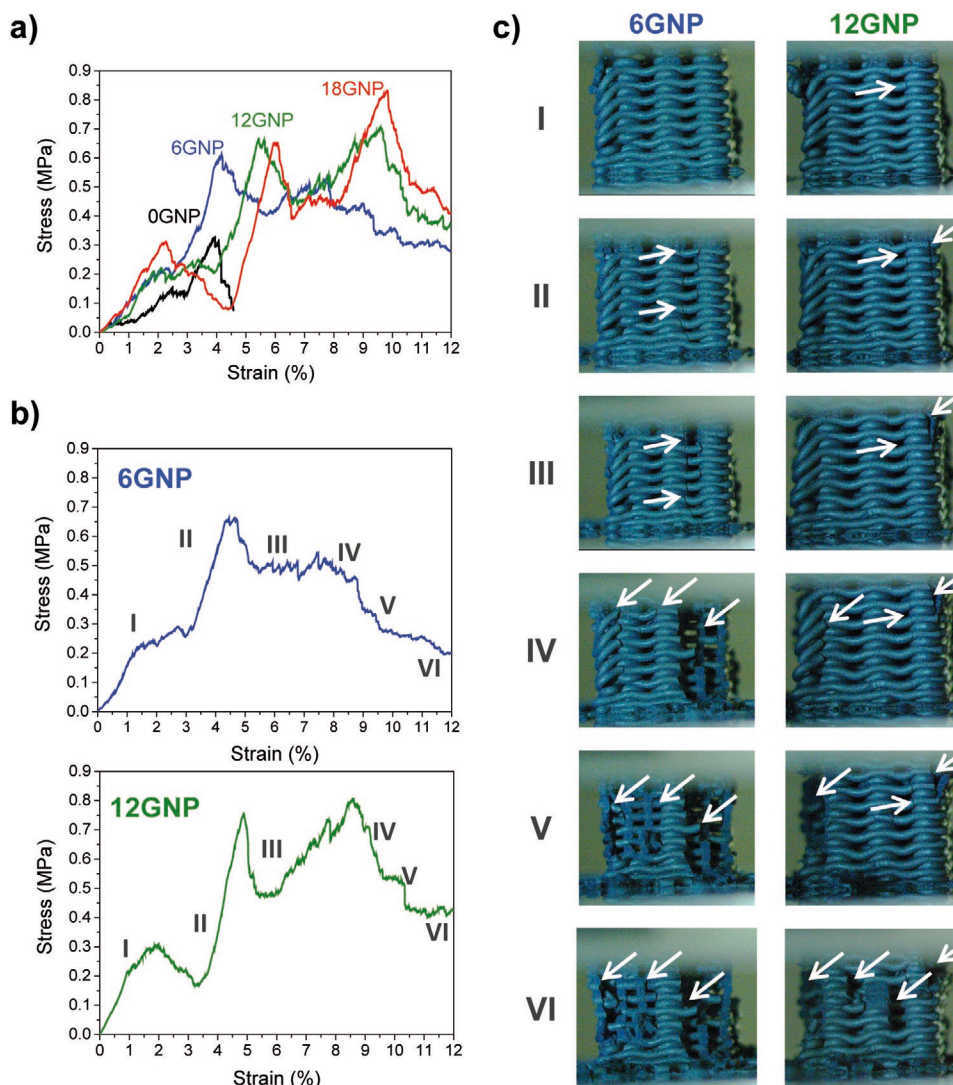


**Figure 8.** a) Representative stress–strain curves for 0GNP, 6GNP, 12GNP, and 18GNP Type 2 scaffolds. b) Examples of stress–strain curves of 6GNP and 12GNP composite scaffolds and c) optical images of the scaffolds simultaneously acquired during the tests for the different regions of the curves (labeled in [b]). Arrows point the cracks formed in the scaffolds during the tests.

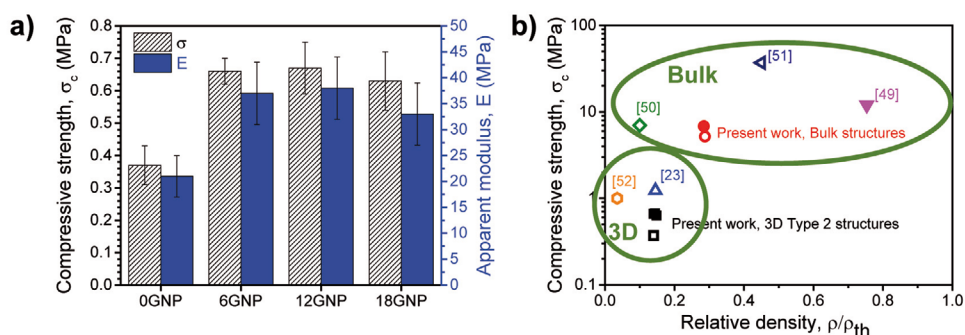


**Figure 9.** a) Apparent elastic modulus ( $E$ ) and compressive strength ( $\sigma_c$ ) versus the GNP content. b) Compressive strength of boehmite-based bulk materials and scaffolds as a function of the relative density ( $\rho/\rho_{th}$ ). The materials have been obtained by different conforming and thermal treatments and full symbols represent those containing carbon-based nanofillers.

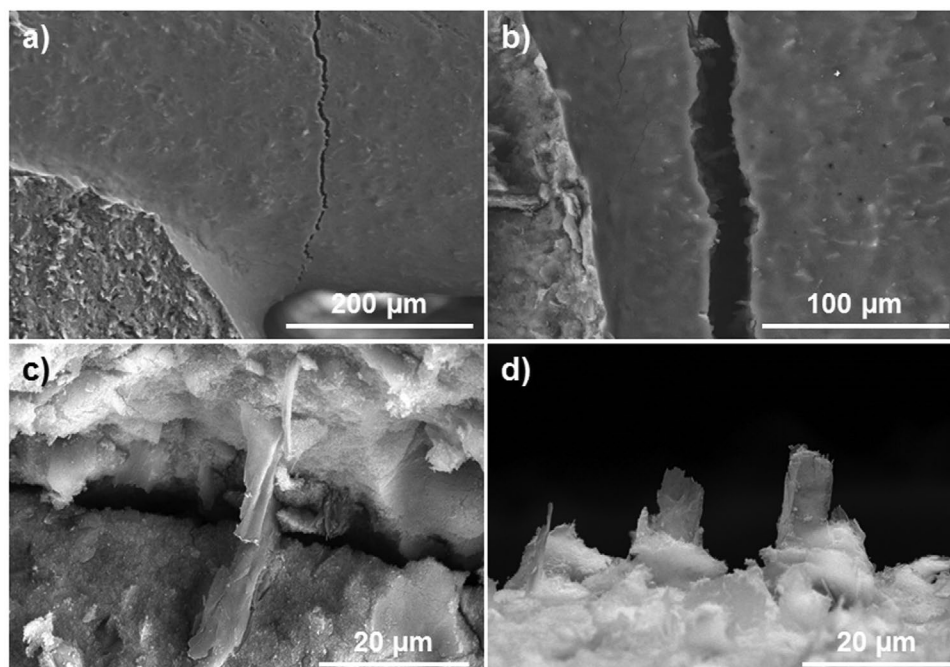


**Figure 10.** FESEM images of the 18GNP fractured scaffold: a) a crushed cell showing a cross-sectional fractured rod and a visible crack developed on the surface of the orthogonal rod; b) a magnified image of this type of surface cracks; c) GNP bridging crack faces; and d) nanoplatelets protruding from a rod fracture surface.

robocasting from highly concentrated boehmite-based aqueous inks that show high shear moduli and yield stress, without any additional printing additives. The storage modulus at high shear stress and the yield stress progressively decrease with the GNP content probably due to the increasing GNP orientation during the test. The transformation of boehmite into  $\gamma\text{-Al}_2\text{O}_3$  takes place during the heat treatment at 500 °C, and a strong interaction between the  $\gamma\text{-Al}_2\text{O}_3$  matrix and the GNP can be inferred from the observed red shifts of the G band position. The developed scaffolds exhibit high porosity (>85%) and include both macropores in the millimeter scale and also mesoporosity ( $\approx 10$  nm size), showing quite high specific surface area ( $100\text{ m}^2\text{ g}^{-1}$ ); the porosity for the interior spanned structure is around 40% but the macroporosity reduces to  $\approx 20\%$  for the covered scaffolds.

The  $\alpha$  and  $\kappa$  values of the bulk reference materials measured by both TPS and laser flash are quite consistent, and significantly increase with the GNP content, being 200% and 310% for  $\alpha$  and  $\kappa$ , respectively, for GNP contents in the 0 to 18 vol% range. The use of scaffolds designed with top and bottom covers allows measuring the thermal properties by the TPS method. The thermal conductivity of the scaffolds increases with the amount of GNP in the same way as bulk materials, but values diminish to 0.7 times that of the rod material due to the presence of macroporosity.

Finally, the developed composite scaffolds display electrical conductivity in the range of  $10^{-3}$ – $10^{-4}$  S  $\text{m}^{-1}$  (approximately eight orders of magnitude higher than the matrix value), and enhanced mechanical properties attributable to the GNP toughening, with increments of the compressive strength and elastic modulus of up to 80%. All these properties are most significant

for applications in the field of catalysis as well as electrical and thermal engineering.

#### 4. Experimental Section

**Materials Processing:** Boehmite powders (AlO(OH), Dispal 11N7-80, SASOL, USA, 220 nm particle size, 30 nm crystallite size, modified with 0.1 wt% of nitric acid) and functionalized GNP (grade N006-010-P, Angstrom Materials Inc., USA, with nominal thickness of 10–20 nm and  $x$ - $y$  dimensions of  $\approx 14$   $\mu\text{m}$ ) were used to prepare  $\gamma\text{-Al}_2\text{O}_3$ -based materials with GNP contents of 0, 6, 12, and 18 vol%. A stable colloidal dispersion of 41 wt% of boehmite in Milli-Q water, which was attained by blade mixing during 180 min, was used as starting suspension to develop highly concentrated inks for both the monolithic  $\gamma\text{-Al}_2\text{O}_3$  material and the  $\gamma\text{-Al}_2\text{O}_3$ /GNP composites. These inks were fabricated by adding to the initial boehmite solution the required amount of the corresponding powders (boehmite and GNP) for having the highest possible solids content, which was 52 wt% in all cases, without compromising the printability of the inks. The inks were homogenized in a planetary centrifugal mixer (AR-250, Thinky Company, Laguna Hills, USA) at 2000 rpm during 2 min.

The flow curves of the different inks were determined with a rheometer (CVO 100 D, Bohlin Instruments, UK) using a cone-and-plate geometry measuring system (diameter: 40 mm; cone angle:  $4^\circ$ ) that was covered with a fitting tool to reduce the evaporation of the ink. The apparent viscosity of the inks was measured as a function of shear rate ( $0.07 < \dot{\gamma} < 100\text{ s}^{-1}$ ) at 30 discrete points with logarithmic spacing, in increasing slope. Additionally, oscillation amplitude sweep tests were performed at a frequency of 1 Hz for the characterization of  $G'$  and  $G''$  of the inks, applying ascending shear stress ( $\tau = 0.5$ – $1000$  Pa) and considering test points with logarithmic spacing. A pre-shearing of  $5\text{ s}^{-1}$  for 30 s, and a 30 s pause to restore the equilibrium was used in all cases before testing.

3D square structures were printed with a three-axis robocasting system (A3200, 3-D Inks LLC, USA) and using a 3D CAD software

(RoboCAD 4.2, 3-D Inks LLC, USA). The inks were loaded into a 3 cm<sup>3</sup> printing syringe and, then, extruded through the nozzle tip of 840 μm inner diameter (Precision Tips; EFD Inc., USA) onto flat alumina substrates following the abovementioned CAD models to build the 3D structures. These scaffolds were left to dry under ambient conditions for 2 weeks and, afterward, 2 days more inside an oven at 100 °C. The dried specimens were thermally treated in a tubular furnace at 500 °C for 2 h under a N<sub>2</sub> flow of 200 kPa.

**Porosity Calculations:** The total porosity of the bulk materials and scaffolds ( $\pi_{\text{total}}$ ) was determined using the geometrical density ( $\rho_{\text{geo}}$ ), assessed from their weights and dimensions, and the theoretical density calculated from the volume fraction and theoretical density of each phase, that is, 3.65 and 2.20 g cm<sup>-3</sup> for  $\gamma$ -Al<sub>2</sub>O<sub>3</sub> and GNP, respectively. The resulting theoretical densities for the  $\gamma$ -Al<sub>2</sub>O<sub>3</sub>/GNP composites were 3.56, 3.48, and 3.38 g cm<sup>-3</sup> for 6, 12, and 18 vol% GNP, respectively.

The macroporosity of the lattices ( $\pi_{\text{latt}}$ ) in the different scaffolds (interior spanned structure in the case of Type 1 scaffolds in Figure 2a) was estimated from the void volume using:

$$\pi_{\text{latt}} = 1 - V_{\text{sol\_latt}}/V_{\text{total\_latt}} = 1 - N_{\text{rod}}^{x-y} \cdot N_{\text{planes}}^z \cdot V_{\text{rod}}/V_{\text{total\_latt}} \quad (4)$$

where the number of rods in the  $x$ - $y$  plane ( $N_{\text{rod}}^{x-y}$ ), the number of  $x$ - $y$  planes in the  $z$  direction ( $N_{\text{planes}}^z$ ), the volume of an individual rod in that plane ( $V_{\text{rod}}$ ), and the volume of the lattice ( $V_{\text{total\_latt}}$ ) were calculated from the scaffold dimensions and its characteristic parameters according to Equations (5)–(7):

$$N_{\text{rod}}^{x-y} = \frac{L_{\text{latt}}}{a} + 1 \quad (5)$$

$$N_{\text{planes}}^z = \frac{H_{\text{latt}}}{h/2} + 1 \quad (6)$$

$$V_{\text{rod}} = \pi \cdot (\varnothing/2)^2 \cdot L_{\text{latt}} \quad (7)$$

$L_{\text{latt}}$  was equal to that of the side length of the structure ( $L$ ) for the Type 2 specimens, but it would be  $L - 4\varnothing$  for the Type 1 specimens with the sidewalls formed by two filaments (Figure 2a). Furthermore, due to the top and bottom covers, the height of the lattice for the Type 1 specimens was reduced to  $H_{\text{latt}} = H - 2 \cdot (h + \varnothing \cdot (1 - \pi/4))$  respecting the height of the scaffold ( $H$ ) because of the two layers at each cap and the overlapping ( $h/2\varnothing = \pi/4$  in the CAD design) of the layer adjacent to the caps. The definite  $\pi_{\text{macro}}$  was, then, calculated for each type of structure by subtracting the volume fraction of solid material associated with the external frame ( $V_{\text{ext}}$ ):

$$\pi_{\text{macro}} = \pi_{\text{latt}} - V_{\text{ext}}/V_{\text{total}} \quad (8)$$

and the porosity of the solid phase forming the rods ( $\pi_{\text{solid}}$ ) was estimated considering

$$\pi_{\text{total}} = \pi_{\text{macro}} + (1 - \pi_{\text{macro}}) \cdot \pi_{\text{solid}} \quad (9)$$

**Materials Characterization:** The full transformation to  $\gamma$ -Al<sub>2</sub>O<sub>3</sub> was confirmed by XRD (Bruker, D8 advance, Bragg-Brentano setup, USA) in ground samples. A TriStar 3000 Equipment (Micromeritics, USA) was used to measure the specific surface area and the pore distribution of the scaffolding materials through the BET and BJH models, respectively, degassing the samples at a lower temperature than that at which they were treated. The characteristic dimensions and shrinkage of the scaffolds at the different processing steps were evaluated by optical and FESEM (Hitachi S-4700, Japan). The microstructure of the rods was studied using the FESEM and confocal micro-Raman spectroscopy (model Alpha300 WITec GmbH, Germany). Raman maps of 20 × 20 μm<sup>2</sup>, with a resolution of 70 × 70 pixel and an acquisition time of 100 ms per spectrum, were recorded using a laser wavelength excitation of 532 nm.

The thermal behavior, that is, the thermal conductivity ( $\kappa$ ), thermal diffusivity ( $\alpha$ ), and heat capacity ( $C_p$ ), of the bulk materials and 3D Type 1 structures were analyzed using the TPS method (model Trident, C-Therm Technologies Ltd., Canada), where a flexible double-sided sensor, which acted both as a heat source for increasing the temperature of the samples and for recording the time-dependent temperature increment, was placed between two identical specimens. These tests were performed at a fixed temperature of 20 °C inside a thermal chamber using 0.01 W of power and times for the regression analysis in the ranges 5–15 and 15–40 s for the bulk materials and the scaffolds, respectively. The top and bottom covers included in these structures assure the close contact between the heat source and the specimen, and also limit possible problems associated to gas turbulences. The size of these samples (30 × 30 × 7.3 mm<sup>3</sup>) was defined by the diameter of the double-sided hot disc sensor used (6 mm). The weight loss associated to absorbed water in the heat treated specimens was evaluated by TGA-DTA (SDT Q600, TA Instruments, USA) using a heating rate of 5 °C min<sup>-1</sup> up to 500 °C under N<sub>2</sub>. The specific heat ( $C_p$ ) of each specimen was measured by DSC (SDT Q600, TA instruments, USA). Four heating-cooling cycles were performed at 10 °C min<sup>-1</sup> to evaluate the effect of the humidity on  $C_p$ .

Type 2 scaffolds were tested under compression with their patterned sides facing compression platens using a universal testing machine (ZwickiLine Z5.0 TS, Zwick-Roell, Germany) with a crosshead displacement rate of 0.1 mm min<sup>-1</sup>. The apparent elastic modulus ( $E$ ) was obtained from the slope of stress-strain curves in the linear elastic region observed after a first stabilization. The compression tests were recorded with a Basler USB camera (model acA1920, Ahrensburg, Germany) acquiring one frame every 2 s. Individual images were then selected to illustrate the behavior of the scaffold at different regions during testing. Fracture surfaces were observed by FESEM. Bulk cylindrical samples (10 mm in diameter and 10.5 mm in height) of 0GNP and 12GNP compositions were also tested under compression using same conditions for having a reference of the rod mechanical properties.

Type 1 specimens were also used for the electrical conductivity measurements. Two silver electrodes were attached on opposite faces of the scaffolds using silver paste (Agar 6302), to assure a good electrical contact, and connected to platinum wires to measure the conductivity in the longitudinal direction relative to the scaffold rods. The electrical conductivity ( $\sigma_e$ ) of the scaffolds was calculated according to the formula  $\sigma_e = D \cdot (R \times S)^{-1}$ , where  $R$  was the electrical resistance of the sample,  $S$  was the electrode surface area, and  $D$  was the distance between the electrodes.

## Supporting Information

Supporting Information is available from the Wiley Online Library or from the author.

## Acknowledgements

This work was supported by the Spanish Government through RTI2018-095052-B-I00 (MICINN/AEI/FEDER, UE) and EIN2020-112153 (MCIN/AEI/10.13039/501100011033) projects, the latter also supported by the European Union through “NextGenerationEU/PRTR”. L.M.-S. acknowledges the financial support from MICINN/AEI/FEDER through the FPI contract Ref. PRE2019-091429 (2019 call). Authors thank Dr. J. J. Moyano and Dr. D. Pérez-Coll for their experimental assistance in the printing process and electrical measurements, respectively.

## Conflict of Interest

The authors declare no conflict of interest.

## Data Availability Statement

The data that support the findings of this study are available from the corresponding author upon reasonable request.

## Keywords

3D printing, alumina, ceramic/graphene composites, direct ink writing, porous materials, strength, thermal conductivity

Received: November 2, 2021

Revised: February 14, 2022

Published online: March 17, 2022

- [1] M. Kuemmel, D. Grosso, C. Boissière, B. Smarsly, T. Brezesinski, P. A. Albouy, H. Amenitsch, C. Sanchez, *Angew. Chem.* **2005**, *117*, 4665.
- [2] Y. Li, C. Peng, L. Li, P. Rao, *J. Am. Ceram. Soc.* **2014**, *97*, 35.
- [3] N. Svarovskaya, E. Glazkova, O. Bakina, S. Kazantsev, A. Lozhkomoiev, M. Lerner, *Recent Pat. Nanotechnol.* **2020**, *14*, 92.
- [4] X. M. Liu, H. X. Xue, X. Li, Z. F. Yan, *Catal. Today* **2010**, *158*, 446.
- [5] Y. Wan, H. Yi, Y. Wang, G. Luo, *Ind. Eng. Chem. Res.* **2018**, *57*, 11636.
- [6] Y. Dong, X. Yu, Y. Zhou, Y. Xu, X. Lian, X. Yi, W. Fang, *Catal. Sci. Technol.* **2018**, *8*, 1892.
- [7] V. S. Semeykina, E. V. Parkhomchuk, A. V. Polukhin, P. D. Parunin, A. I. Lysikov, A. B. Ayupov, S. V. Cherepanova, V. V. Kanazhevskiy, V. V. Kaichev, T. S. Glazneva, V. V. Zvereva, *Ind. Eng. Chem. Res.* **2016**, *55*, 3535.
- [8] W. Yang, F. Ling, H. Zhang, S. Wang, Z. Shen, *Chem. Lett.* **2019**, *48*, 1274.
- [9] A. Zocca, P. Colombo, C. M. Gomes, J. Günster, *J. Am. Ceram. Soc.* **2015**, *98*, 1983.
- [10] J. A. Lewis, J. E. Smay, J. N. Stuecker, J. Cesarano, *J. Am. Ceram. Soc.* **2006**, *89*, 3599.
- [11] Y. Lakhdar, C. Tuck, J. Binner, A. Terry, R. Goodridge, *Prog. Mater. Sci.* **2021**, *116*, 100736.
- [12] A. D. Salazar-Aguilar, A. Quintanilla, P. Lopez, C. Martinez, S. M. Vega-Díaz, J. A. Casas, P. Miranzo, M. I. Osendi, M. Belmonte, *ACS Appl. Mater. Interfaces* **2022**, *14*, 920.
- [13] Y. Li, Z. Y. Fu, B. L. Su, *Adv. Funct. Mater.* **2012**, *22*, 4634.
- [14] T. D. Ngo, A. Kashani, G. Imbalzano, K. T. Nguyen, K. T. D. Hui, *Composites, Part B* **2018**, *143*, 172.
- [15] U. Scheithauer, E. Schwarzer, T. Moritz, A. Michaelis, *J. Mater. Eng. Perform.* **2018**, *27*, 14.
- [16] Z. Chen, Z. Li, J. Li, C. Liu, C. Lao, Y. Fu, C. Liu, Y. Li, P. Wang, Y. He, *J. Eur. Ceram. Soc.* **2019**, *39*, 661.
- [17] Y. Li, Z. Feng, L. Huang, K. Essa, E. Bilotti, H. Zhang, T. Peijs, L. Hao, *Composites, Part A* **2019**, *124*, 105483.
- [18] M. Pelanconi, M. Barbato, S. Zavattoni, G. L. Vignoles, A. Ortona, *Mater. Des.* **2019**, *163*, 107539.
- [19] Y. Du, J. Chen, Q. Meng, Y. Dou, J. Xu, S. Z. Shen, *Vacuum* **2020**, *178*, 109384.
- [20] C. Ramírez, M. Belmonte, P. Miranzo, M. I. Osendi, *Materials* **2021**, *14*, 2071.
- [21] K. S. Novoselov, V. I. Falko, L. Colombo, P. R. Gellert, M. G. Schwab, K. Kim, *Nature* **2012**, *490*, 192.
- [22] P. Miranzo, M. Belmonte, M. I. Osendi, *J. Eur. Ceram. Soc.* **2017**, *37*, 3649.
- [23] C. Ramírez, M. Belmonte, P. Miranzo, M. I. Osendi, *Materials* **2021**, *14*, 2111.
- [24] A. M'barki, L. Bocquet, A. Stevenson, *Sci. Rep.* **2017**, *7*, 6017.
- [25] X. Zhang, W. Huo, J. Liu, Y. Zhang, S. Zhang, J. Yang, *J. Eur. Ceram. Soc.* **2020**, *40*, 930.
- [26] H. Xie, X. Yang, P. Liu, X. Xu, Z. Zhou, W. Zhao, Z. Shen, *J. Eur. Ceram. Soc.* **2021**, *41*, 6634.
- [27] Y. Zheng, X. Luo, J. You, T. Li, Q. Hou, *J. Am. Ceram. Soc.* **2021**, *104*, 1902.
- [28] C. Huo, X. Tian, C. Chen, J. Zhang, Y. Nan, Q. Zhong, X. Huang, J. Hu, D. Li, *J. Eur. Ceram. Soc.* **2021**, *41*, 4231.
- [29] K. Bhowmik, A. Chakravarty, S. Bysakh, G. De, *Energy Technol.* **2016**, *4*, 1409.
- [30] A. Iqbal, S. Sajjad, S. A. K. Leghari, *ACS Appl. Nano Mater.* **2018**, *1*, 4612.
- [31] M. Taleb, R. Ivanov, S. Bereznev, S. H. Kazemi, I. Hussainova, *Microchim. Acta* **2017**, *184*, 897.
- [32] A. Quintanilla, J. Carbajo, J. A. Casas, P. Miranzo, M. I. Osendi, M. Belmonte, *Catal. Today* **2020**, *356*, 197.
- [33] M. Lorenz, B. Dietemann, L. Wahl, C. Bierwisch, T. Kraft, H. Kruggel-Emden, N. Travitzky, *J. Eur. Ceram. Soc.* **2020**, *40*, 811.
- [34] B. Roman-Manso, F. M. Figueiredo, B. Achiaga, R. Barea, D. Perez-Coll, A. Morelos-Gomez, M. Terrones, M. I. Osendi, M. Belmonte, P. Miranzo, *Carbon* **2016**, *100*, 318.
- [35] A. Nistal, E. Garcia, D. Pérez-Coll, C. Prieto, M. Belmonte, M. I. Osendi, P. Miranzo, *Carbon* **2018**, *139*, 556.
- [36] C. Ramírez, E. Garcia, E. Barrena, A. De Pablos, M. Belmonte, M. I. Osendi, P. Miranzo, C. Ocal, *Carbon* **2019**, *153*, 417.
- [37] A. Das, B. Chakraborty, A. K. Sood, *Bull. Mater. Sci.* **2008**, *31*, 579.
- [38] M. A. Bisset, M. Tsuji, H. Ago, *Phys. Chem. Chem. Phys.* **2014**, *26*, 11124.
- [39] G. Bottari, M. A. Herranz, L. Wibmer, M. Volland, L. Rodriguez-Perez, D. M. Guldi, A. Hirsch, N. Martin, F. D'Souza, T. Torres, *Chem. Soc. Rev.* **2017**, *46*, 4464.
- [40] J. Li, X. Li, K. Wu, D. Feng, T. Zhang, Y. Zhang, *Int. J. Coal Geol.* **2017**, *179*, 253.
- [41] J. Xiang, L. T. Drzal, *Carbon* **2011**, *49*, 773.
- [42] J. J. Calvin, M. Asplund, Y. Zhang, B. Huang, B. F. Woodfield, *J. Chem. Thermodyn.* **2017**, *112*, 77.
- [43] W. Pabst, T. Uhlířová, E. Gregorová, A. Wiegmann, *J. Eur. Ceram. Soc.* **2018**, *38*, 2694.
- [44] S. Y. Chung, D. Stephan, M. A. Elrahman, T. S. Han, *Constr. Build. Mater.* **2016**, *111*, 529.
- [45] H. Prajapati, D. Ravoori, R. L. Woods, A. Jain, *Addit. Manuf.* **2018**, *21*, 84.
- [46] D. Ravoori, L. Alba, H. Prajapati, A. Jain, *Addit. Manuf.* **2018**, *23*, 132.
- [47] A. Elkholy, M. Rouby, R. Kempers, *Prog. Addit. Manuf.* **2019**, *4*, 497.
- [48] D. M. Codorníu, J. J. Moyano, M. Belmonte, M. I. Osendi, P. Miranzo, *Open Ceram.* **2020**, *4*, 100028.
- [49] M. Ikram, Z. Tao, J. Ye, H. A. Qayyum, X. Sun, J. Xu, *RSC Adv.* **2018**, *8*, 8329.
- [50] Z. R. Ismagilov, R. A. Shkrabina, N. A. Koyabkina, *Catal. Today* **1999**, *47*, 51.
- [51] A. Samini, M. Zakeri, B. Maleki, D. Mohebbi-Kalhari, *Particuology* **2015**, *21*, 74.
- [52] X. Zhang, W. Huo, J. Liu, Y. Zhang, S. Zhang, J. Yang, *J. Eur. Ceram. Soc.* **2020**, *40*, 930.
- [53] V. Middelkoop, A. Vamvakeros, D. de Wit, S. D. M. Jacques, S. Danaci, C. Jacquot, Y. de Vos, D. Matras, S. W. T. Price, A. M. Beale, *J. CO2 Util.* **2019**, *33*, 478.
- [54] S. Lawson, X. Lin, H. Thakkar, A. A. Rownagli, F. Rezaei, *Chem. Rev.* **2021**, *121*, 6246.
- [55] C. Ramírez, Q. Wang, M. Belmonte, P. Miranzo, M. I. Osendi, B. Sheldon, N. P. Padture, *Scr. Mater.* **2018**, *149*, 40.
- [56] R. Brezny, D. Green, in *Materials Science and Technology – A Comprehensive Treatment*, Vol. 11 (Eds: R. W. Cahn, P. Haasen, E. J. Kramer), Wiley-VCH, Weinheim, Germany **2005**, pp. 463–516.